Electronic Supplementary Material (ESI) for Nanoscale.

Supplementary Information to

Local surface conductivity of transition metal oxides mapped with true atomic resolution

C. Rodenbücher, G. Bihlmayer, W. Speier, J. Kubacki,
M. Wojtyniak, M. Rogala, D. Wrana, F. Krok, K. Szot

I. The LC-AFM technique

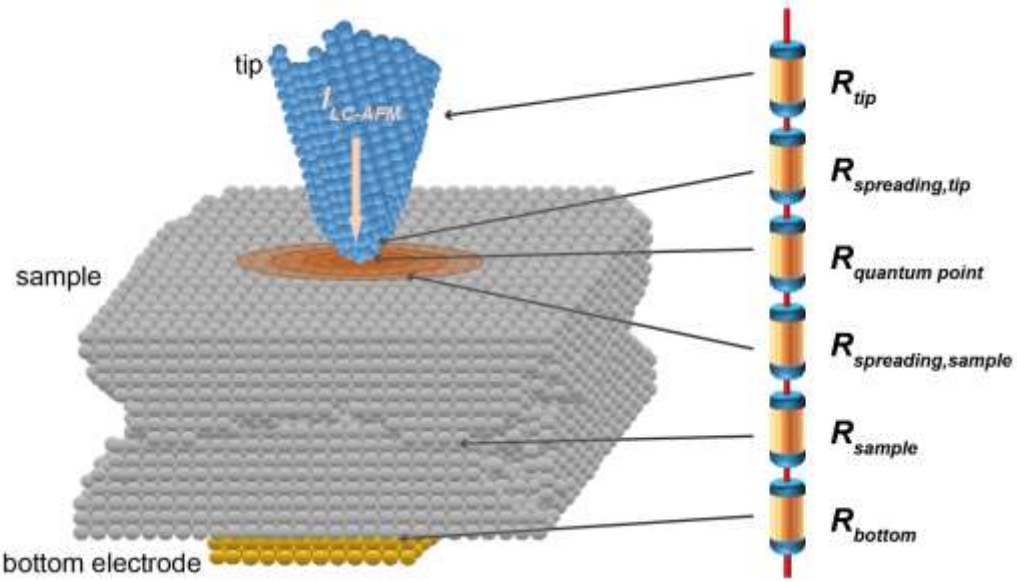

Fig. S1.1. Configuration of a LC-AFM measurement with a metallic tip in galvanic contact to the sample and equivalent circuit illustrating the contribution of different resistances to the current.

In order to understand the origin of the measured current signal in LC-AFM we have a closer look on the electrical contact between tip and sample. Since the positioning of the tip is decoupled from the adjustment of the height by a force feedback loop e.g. by measuring the position of the cantilever by piezoelectric, interferometric or optical lever method, the apex of the tip is in galvanic contact with the sample enabling a direct current flow through the hybridized orbitals of the last metallic tip atom and the contacting sample atom on the surface. In consequence, when describing the system in an equivalent circuit, the total resistance is composed by the resistances of the tip, the sample and the contact resistances at the tip-sample and sample-bottom electrode interface[1].

$$R_{total} = R_{tip} + R_{contact} + R_{sample} + R_{bottom} \qquad \text{(Eq. 1)}$$

The contact resistance itself can be separated in three resistances namely the spreading resistance and the quantum point resistance as explained in the following.

$$R_{contact} = R_{spreading,tip} + R_{quantum\,point} + R_{spreading,sample} \qquad \text{(Eq. 2)}$$

In general, three different situations can be distinguished at the contact between a metallic tip and a sample as illustrated in the energy diagrams (Fig. S1.2). If the sample is metallic, an ohmic contact is formed but still the majority of the voltage would drop at the contact due to the geometry resulting in a spreading resistance. In the simplest case, when the contact area is relatively large as used in scanning spreading resistance microscopy (SSRM)[2] the spreading resistance is given by the (Maxwell formula)[3]

$$R_{spreading} = R_{spreading}^{tip} + R_{spreading}^{sample} = \frac{\rho_{tip}}{4 \cdot a} + \frac{\rho_{sample}}{4 \cdot a} \qquad \text{(Eq. 3)}$$

where ρ is the resistivity and a is the radius of the contact area.
When shrinking the electrical contact area below 1 nm^2 and eventually towards a monoatomic contact needed for LC-AFM measurements with atomic resolution, the Maxwell formula is not valid anymore since ballistic transport occurs as described by the Landauer-Büttiker formula[4]. In the limit of a quantum point contact with one conductance channel, the resistance is given by the inverse of the conductance quantum G_0.

$$R_{quantum\ point} = \frac{1}{G_0} = \frac{h}{2e^2} = 12.9\ \text{k}\Omega \qquad \text{(Eq. 4)}$$

Taking this into account, the contact resistance for small contacts can be calculated by the Sharvin formula[5], which can be expressed using the electron mean free path λ under the assumption that the Fermi wavelength is much smaller than the contact radius and that the spreading resistance of the tip is much smaller than that of the sample.

$$R_{contact} = \frac{4\,\rho\lambda}{3\pi a^2}\ . \qquad \text{(Eq. 5)}$$

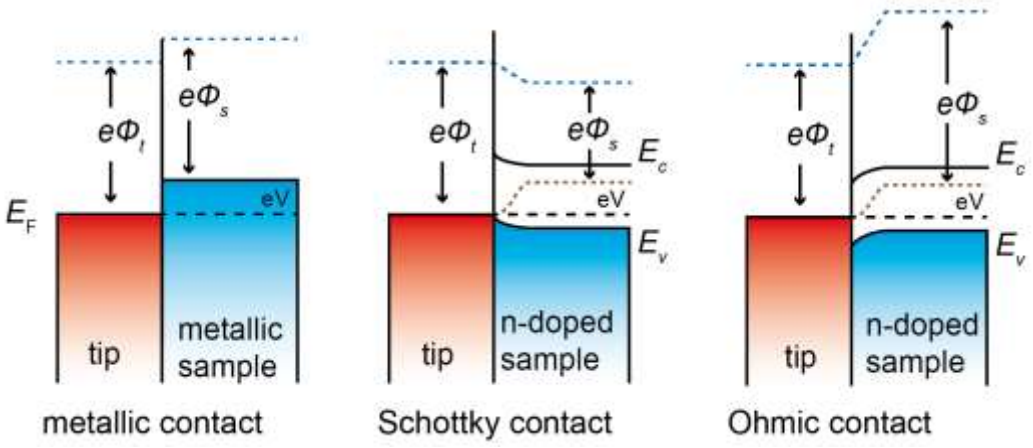

Fig. S1.2. Simplified energy diagrams of the contact between a metallic tip and a metallic (left) and an n-doped sample with different work functions.

Using these formulas, the resistances of surfaces forming an ohmic contact with the tip can be calculated. However, if the sample is a semiconductor (n-doped), the contact can also be rectifying depending on the work functions[6] of metallic tip and semiconductor (Fig. S1.2). If the work function of the semiconductor is smaller than the work function of the metal, an energy barrier is formed leading to a rectifying behaviour[7]. This barrier not only depends on the difference in work function between metal and semiconductor (Schottky barrier) but is also influenced by surface states due to dangling bonds on the surface or to defects and impurities (Bardeen barrier). In order to calculate the current between tip and sample, which is related to a tunnelling process through the barrier, much higher computational effort has to be made[8] in particular since the extrinsic contributions to the barrier strongly depend on the sample preparation and thus may be laterally inhomogeneous. Additionally, it has to be noted that the elaboration of a profound theory for LC-AFM that is able to predict the current between tip and sample from ab initio calculations remains a challenging task for future research.

The consideration above illustrates that analysing and understanding the current in LC-AFM is quite complex. For highly conducting samples in most cases only the contract resistance is relevant and the other series resistances can be neglected causing the entire potential to drop directly at the tip-surface contact This allows for a straight-forward calculation of the surface resistivity from the measured current. If the sample is a poor conductor however, the series resistances may play an important role and thus the voltage drop over the contact resistance is smaller than the externally applied voltage making the extraction of the surface resistivity difficult.

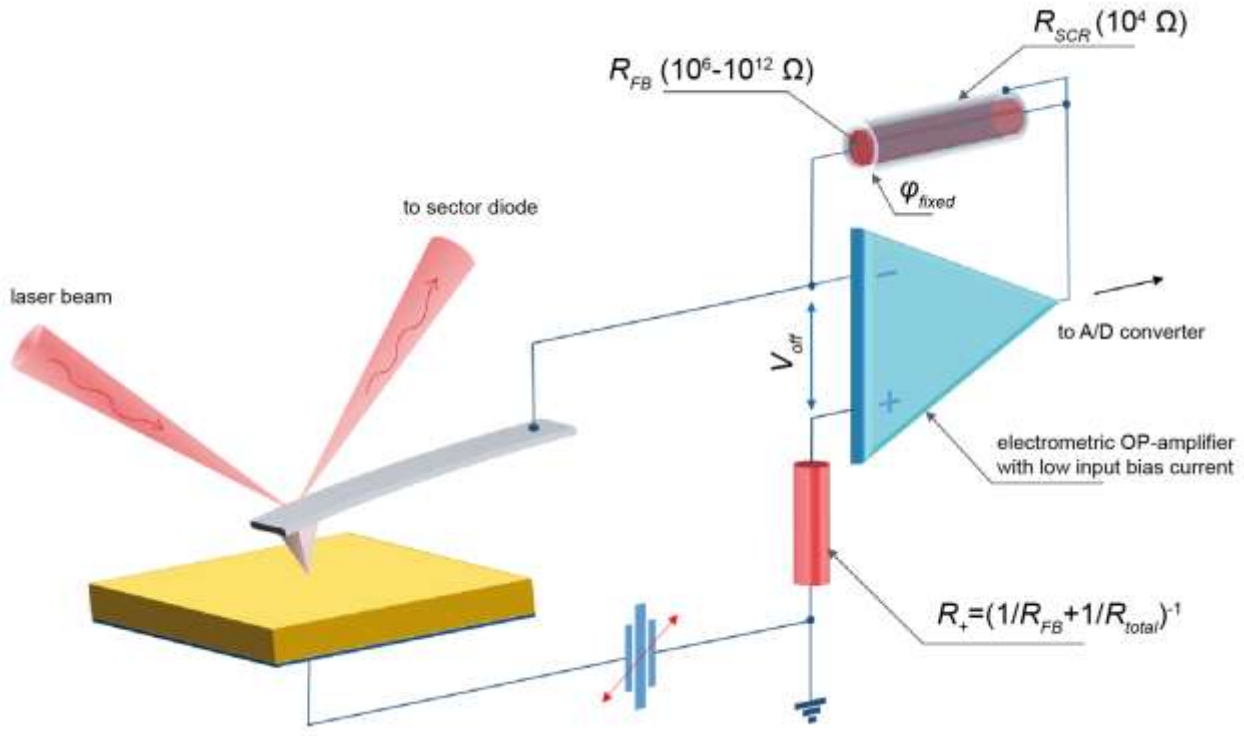

Fig. S1.3. Setup of the transimpedance amplifier used for measuring the current in LC-AFM

In order to obtain LC-AFM maps with high sensitivity, the most decisive step is the measurement of the current that will be explained in more detail in the following. As depicted in Fig. S1.3, a voltage is applied between tip and sample and the current is fed in a transimpedance amplifier with virtual ground[9] that is realized by combining an operational amplifier with a feedback resistor R_{FB}. The output voltage V_{out} that is than recoded by an analogue/digital converter is proportional to the current $I_{LC\text{-}AFM}$.

$$V_{out} = -R_{FB} \cdot I_{LC\text{-}AFM} \qquad \text{(Eq. 6)}$$

The value of the feedback resistor is adjusted to the measurement range and is typically of order of 10^6 Ω to 10^{12} Ω. The current maps shown in the main part of this paper were obtained using a value of R_{FB} = 10^7 Ω. When measuring samples with much smaller conductivity e.g. undoped $SrTiO_3$ with low oxygen vacancy concentration[10], a much higher feedback resistance has to be selected. Hence, great care has to be taken to select operational amplifiers and resistances with very low noise and to reduce parasitic capacitances. For this purpose we applied equipotential screening[11] by embedding the feedback resistor R_{FB} in a material with low resistance R_{SCR}.
Since ultra-small voltages in the range of several mV are used to measure the conductivity of the reduced oxide surface showing locally metallic conductivity, the influence of the offset voltage of the operational amplifier in the I/V converter has to be taken into account. Even in high precision amplifiers, the offset can be of several mV thus being in the same range than the externally applied voltage. Hence, a careful offset calibration has to be performed to minimize the error of the measurement.

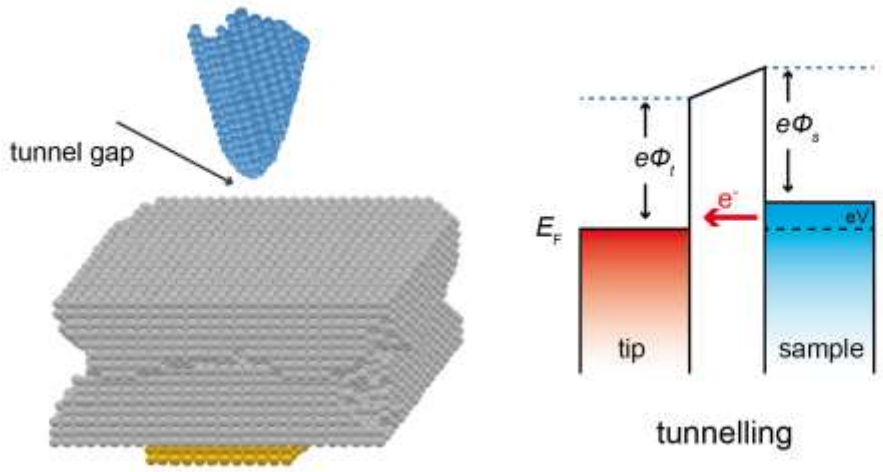

Fig. S1.4. Illustration of the STM technique and energy diagram for positive tip bias.

As comparison to the LC-AFM technique we would like to briefly revisit the STM technique which is also widely used for the investigation of electrical properties of surfaces. In the topography mode of STM, the tip height is adjusted by a feedback loop keeping the tunnel current between tip and sample constant and thus allows for an estimation of the topography on samples with sufficient high surface conductivity. Since the tip is not in direct contact with the sample, only a tunnel current is flowing. Regarding an equivalent circuit of this setup one has to consider both the tunnel resistance and the capacitance between tip and sample. The simplified energy diagram (Fig. S1.4) illustrates that tip and sample are separated electrically but since (in the case of positive tip voltage) the energy of the sample is lifted by the applied voltage, electrons can tunnel if the gap is in the

range of a few Å. Theoretically, the tunnel current can be described using perturbation theory[12, 13] taking into account the convolution of the electronic densities of states of tip and sample.

In particular on transition metal oxides, it was found that the surface conductivity shows significant lateral variation. Hence if one would conduct STM measurements on such kind of surfaces, it would only work on those areas providing a tunnel current being high enough for a successful operation of the feedback loop. But if the tip would be approached to an area of the surface, where the conductivity is orders of magnitude lower than in the good conducting regions, a tip crash would occur immediately as illustrated in Fig. S1.5. To avoid this problem, a typical approach in the surface science community is to generate a reconstructed surface with homogeneous conductivity by repeated steps of annealing and ion bombardment[14]. While this opens up various possibilities to investigate fundamental physical phenomena such as molecular adsorption it only reflects an artificial surface and hence it would be difficult to transfer the results to surfaces from natural or as received Verneuil grown crystals that are used for applications and device production. Hence we would like to promote the LC-AFM technique as method of choice for the investigation and analysis of oxide surfaces with lateral variations in surface conductivity since here the height control is decoupled from the current measurement.

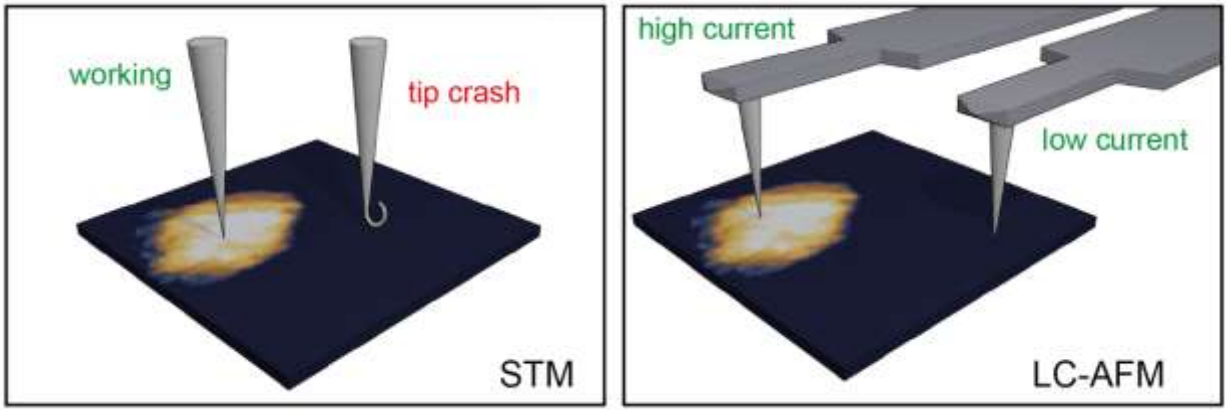

Fig. S1.5. Illustration of the difference between STM and LC-AFM when measuring surfaces with laterally inhomogeneous conductivity.

The observation of atomic resolution in current while performing a contact mode experiment using a relatively broad tip raises the question of the nature of the tip sample contact. According to the Hertz formula, the mechanical contact area can be estimated using the applied force *Fc* (about 30 nN), the radius of the tip R_{tip} (about 15 nm), and Young's moduli E_i and Poisson ratios ν_i of tip and sample (e.g. TiO_2)[15]:

$$A_c = \pi \left(F_c R_{tip} \frac{3}{4} \left(\frac{1-\nu_1}{E_1} + \frac{1-\nu_2}{E_2} \right) \right)^{\frac{2}{3}} \qquad \text{(Eq. 7)}$$

A moderate estimate of the mechanical contact area yields values in the range of 5-8 nm^2. However, it can clearly be seen in LC-AFM measurements that the resolution in current maps is significantly higher than the resolution in topography. Hence we can conclude that the effective electrical contact area is much smaller than the mechanical contact area.

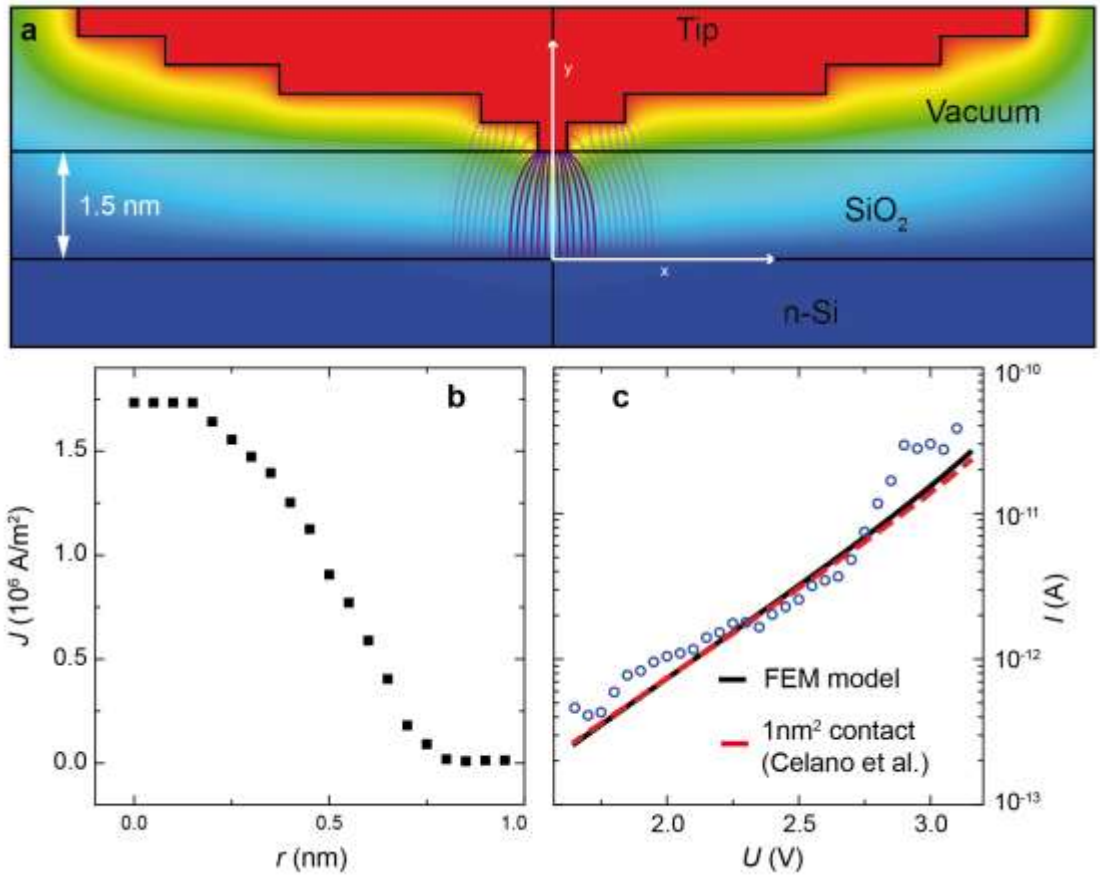

Fig. S1.6. FEM simulation of the contact between the AFM tip and a SiO_2 layer (a). Calculated current density as function of the distance from the centre (b). Comparison of the measured tunnel current with our FEM model and the model presented by Celano et al.

As a convenient method for the estimation of the effective electrical contact area between a tip operated in contact-mode and sample Celano et al.[16] have proposed the measurement of the tunnel current through a thin dielectric SiO_2 layer. According to the work of Frammelsberger et al.[15] this allows for the calculation of the effective contact area. Using this approach we characterized our tips on a 1.5 nm thick SiO_2 layer on top of n-doped Si. The measured tunnel current is shown as blue dots in Fig. S1.6c and corresponds to the expected tunnel current through an oxide with an effective electrode area of A_{eff} = 1 nm^2. Following the method of Celano et al. this theoretical current (red line in Fig S1.6c) was calculated using the formula Eq. 8 based on Fowler-Nordheim tunnelling[15].

$$J = \frac{q^3 m_e}{16\,\pi\,\hbar\,m_{ox}}\left(\frac{V_{ox}}{d_{ox}}\right)^2 \frac{1}{\Phi_B}\exp\left(-\frac{4}{3}\frac{\sqrt{m_{ox}}}{q\,\hbar}\Phi_B{}^{3/2}\frac{d_{ox}}{V_{ox}}\left(1-\left(1-\frac{q\,V_{ox}}{\Phi_B}\right)^{3/2}\right)\right) \qquad \text{(Eq. 8)}$$

$$I = J \cdot A_{eff} \qquad \text{(Eq. 9)}$$

Here, J is the current density, V_{ox} is the voltage across the oxide and d_{ox} is the thickness of the oxide.

m_{ox} is the electron mass in the SiO_2 layer and m_e is the free electron mass. ħ is the reduced Planck constant, q the electron charge, Φ_B is the barrier height and I is the tunnelling current.
In this description however, it is assumed that electron transport takes place exclusively in the circular contact area between tip and oxide. Since a LC-AFM measurement with atomic resolution would not be possible with such a large contact area of 1 nm^2, we argue in the following that also the assumption of a monoatomic tip-sample contact would be in agreement with the measured tunnelling current. Therefore, we conducted a simulation using the finite element method (FEM) implemented in the Ansys software. As shown in Fig. S1.6a, we assumed a metallic tip with one atom at the apex following the geometric estimation of the atomic structure of a tip with 20 nm radius being in contact with a SiO_2 layer. We calculated the potential distribution shown in false colours in Fig. S1.6a and the electron trajectories between tip and substrate shown in purple. For each trajectory we calculated the real distance that the electrons would have to travel during the tunnelling event and calculated the current density as function of the distance r from the centre using Eq. 8 while the origin of our coordinate system was fixed to the interface between substrate and oxide. It can be seen in Fig. S1.6b that the maximum of the current density is located exactly below the tip-oxide contact but that there are also significant contributions at larger distances due to the curved shape of the electron trajectories. Additionally there is also a small contribution from electrons tunnelling from the second atomic layer of the tip through the vacuum gap and the oxide to the substrate. For the sake of simplicity we only took into account the distance of these electron trajectories and still applied Eq. 8 and did not consider that these tunnelling event would be in fact a two-layer problem. The contribution of tunnelling from the second atomic layer of the tip to the total current is well below 10 % and thus does not play a significant role. To estimate the total current I we calculated the current of each trajectory while due to the rotational symmetry of the problem, the corresponding areas for each trajectory have the form of a ring.

$$I = \sum_i J(d(r_i)) \cdot \pi({r_i}^2 - {r_{i-1}}^2) \qquad \text{(Eq. 10)}$$

The resulting total current is plotted in Fig. S1.6c as function of the distance from the origin in x-direction (black line). It can be seen that it is also identical to the calculation of Celano et al. for an effective emission area of 1 nm^2. This shows that our assumption of a monoatomic tip-sample contact can be brought into agreement to the measurement of tunnel currents through a dielectric. If we then would perform an LC-AFM measurement of a material with higher conductivity such as HOPG or the locally conducting oxides shown in the main text, the current would be confined by the galvanic contact between the topmost atom of the tip and the sample allowing for atomic resolution. Additionally any tunnelling current from the second layer of the tip would be orders of magnitude lower than the direct current and would not disturb the measurement. This is confirmed by analysing local I-V curves measured when the tip was in contact to HOPG revealing an ohmic behaviour with linear dependence between current and voltage after tip cleaning (cf. Fig. S3d).
In summary we have shown that a monoatomic tip-sample contact is not in contrast to estimation of the emission area during tunnelling measurements which together with the fact that we could clearly resolve features on the atomic scale on HOPG lets us state that true atomic resolution in LC-AFM measurements is possible with standard tips used for contact-mode.

On the other hand, it is rather unrealistic to assume that the total mechanical force of several tens of nN would be transmitted only via a single atom at the apex of the tip when scanning with a speed of several hundred nanometres per second. As stated above, a more realistic mechanical

contact area would be in the range of several nm^2. To understand this difference, we could imagine that the mechanical contact is realized by non-conducting parts of the tip such as adsorbates that then could even serve as a kind of lubricant. In order to rationalize this idea, we investigated the tips in more detail using electron microscopy. It can be seen in Fig. S1.7 that the apex of the tip is relatively broad consisting of one single grain with a diameter of 10-20 nm. However, after prolonged exposure to the electron beam over several minutes we saw that the image was changing. Starting from the upper part of the tip, an adsorbate drop evolved (Fig. S1.7d) that then proceeded towards the apex (Fig. S1.7e). This illustrates that adsorbates on the PtIr coating were present. A further confirmation for the role of adsorbates was found using LC-AFM investigations of the PtIr coating of the cantilever chip. Here we basically scanned one AFM chip by another. Under ambient air conditions, it can be seen that the inner regions of the crystallites show a high conductivity while the grain boundaries have much lower conductivity indicating the agglomeration of adsorbates there. After annealing the tip at 175 °C under vacuum conditions for 1 h, which is a typical preparation step before conducting measurements in UHV, the conductivity in average was found to be higher but still the grain boundaries showed lower conductivity that the grains illustrating that adsorbates were still present along of grain boundaries. This could indicate that the grain boundaries serve as a kind of reservoir for adsorbates that could make a mechanical contact between tip and sample with a relatively large contact area while the electrical contact being relevant for current flow in LC-AFM could be confined to one single atom as we have shown in the main text.

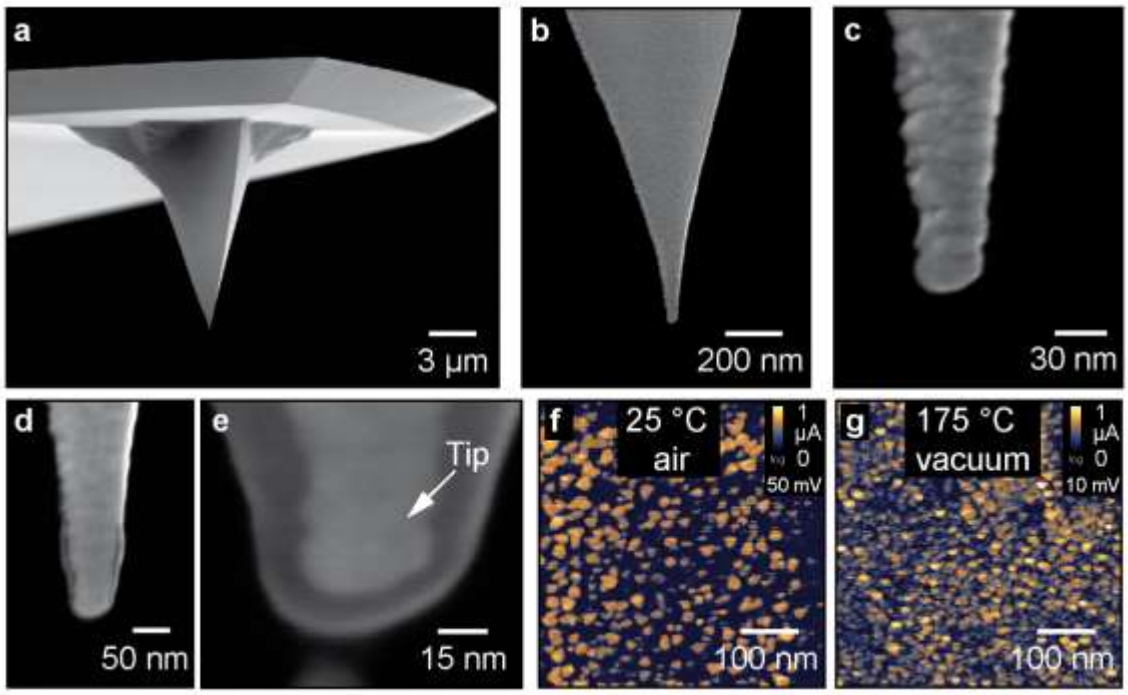

Fig. S1.7. Investigations of the tips. (a-c) Electron microscopy of the standard contact mode tips Nanosensors PPP ContPt used for LC-AFM investigations. (d-e) Apex of the tips after prolonged exposure to the electron beam showing the evolution of an adsorbate shell. (f) LC-AFM images of the PtIr coated cantilever chip before and after (g) annealing in vacuum.

II. DFT simulations

In order to gain insight into the spatial distribution of the local density of states close to oxygen vacancies in the TiO_2 (110) surface we performed calculations using DFT in the generalized gradient approximation[17] with corrections as proposed by Park et al.[18]. In this study, the full-potential linearized augmented plane wave method as implemented in the Fleur-code was used. We simulated oxygen vacancies at the surface and/or below the (110) surface in a 3×2 in-plane supercell of film with nominal thickness of 10 unit cells. The vacancies create in-gap states at the bottom of the conduction band. All atomic positions were allowed to relax resulting in ionic displacements that add to the screening of the electrons in these states. This leads, even at $T = 0$ K, to relatively well localized states characterizing the defects. The relaxation and electronic structure for the surface defect is very similar to the results obtained by Morgan and Watson[19]. As shown in the main text, we used the calculation of a single surface vacancy and a single subsurface vacancy to generate a larger vacancy cluster by superposition of the LDOS. As justification for this approach at first we calculated a cell containing both, a surface and a subsurface vacancy as shown in Fig. S2. The simulation shows in the upper panel the local density of states of a TiO_2 (110) surface with two oxygen vacancies in a region of 270 meV around the Fermi level. The corresponding 3×2 in-plane supercell is shown below with oxygen atoms indicated as large, red spheres and titanium as small, grey ones. Vacancy positions are marked with empty circles. The simulation shows that the LDOS can be regarded as linear superposition of the LDOS calculation of single surface and surface vacancies (see main text). This justifies the simulation of larger defect clusters by superposition, at least if the vacancies are not direct neighbours. This possibility was excluded in our thus generated image of the LDOS of the defect clusters.

The comparison of the LDOS, as obtained in DFT calculations, with the experimentally obtained LC-AFM conductance maps certainly needs some justification. In contrast to scanning tunnelling microscopy, where this procedure is well known as Tersoff-Hamann model[20], in this method it is rather unrealistic to assume that the tip and sample wavefunctions are almost unperturbed in the course of the scanning procedure. Therefore, in the case where this perturbation is of the same order of magnitude as the conductance variation (e.g. on a metallic surface), such approximation will not be appropriate. In our case, i.e. a Pt tip in contact with a TiO_2 surface, the interaction can induce states in the conduction band of the sample[21] but this alone will not lead to local conductivity without the presence of oxygen vacancies that form pathways to the electrode[22]. Only when a connection to the vacancy-induced states in the surface is established, a significant current can flow. The resolution obtained in the LC-AFM map is, therefore, also limited by the length scale of the screening of the local field around the tip that is fortunately quite effective in the investigated oxides.

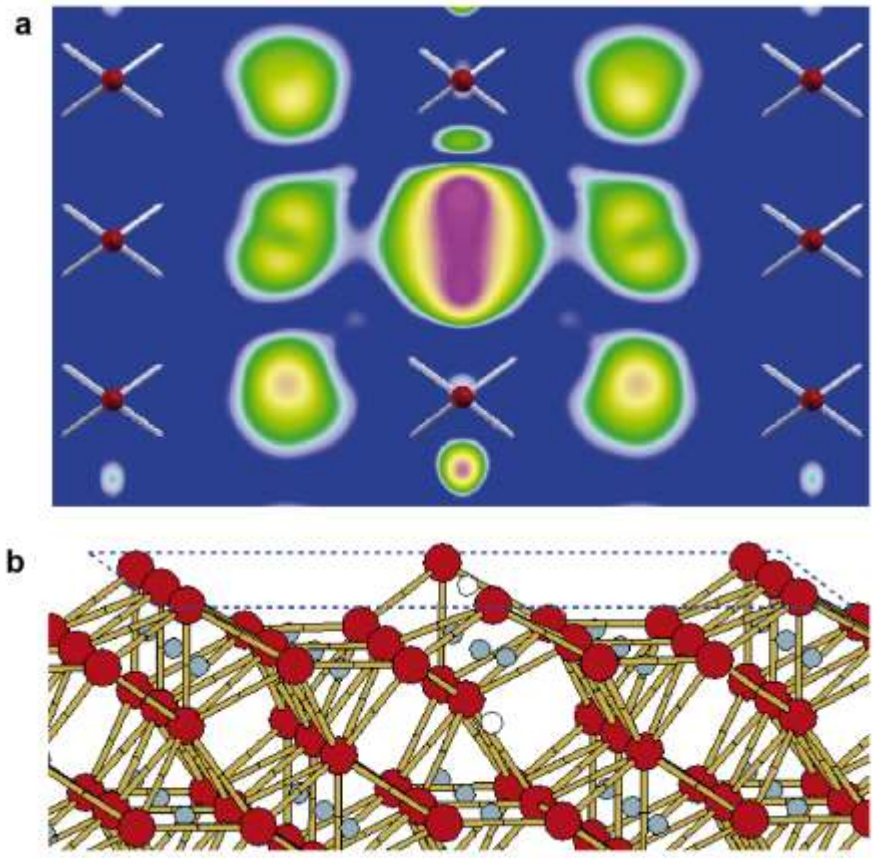

Fig. S2. (a) LDOS simulation of a TiO_2 (110) surface with one surface and one subsurface vacancy. (b) Corresponding ball-and stick model with Ti in grey and oxygen in red.

III. Investigation of HOPG

As standard material for scanning probe microscopy, HOPG was used and we were able to map single surface defects as described in the main text indicating the presence of true atomic resolution. Here, we intend to illustrate the variety in the measurement of local current that may help to understand the mechanism of local conductivity in more detail. As shown in Fig. S3a and S3b current images of two different types revealing either a hexagonal honeycomb structure or a trigonal structure can be obtained. This effect is known from STM investigations and it was concluded that the coupling between the topmost layer and the rest of the crystal is responsible for the different observed structures[23]. In case of a decoupled graphene sheet on top of the crystal a hexagonal symmetry is expected while the trigonal symmetry was found to be indicative for compact graphite[24].

Regarding the absolute current values in Fig. S3a and S3b it is striking that they are relatively low for a measurement of the direct current. Assuming that the current would be mainly determined by the resistance of the monoatomic point contact between the metallic tip and the HOPG having high in-plane conductivity, one would expect a resistance close to 13 kΩ which is the inverse of the conductance quantum[25]. This indicates that the measured current was probably not a direct current between tip and sample but that the adsorbate layer hindered the current flow either by causing a tunnelling through the layer or by establishing a space charge layer. We illustrated this situation in Fig. S3e. In this case the measuring mode would be similar to STM in constant height mode with optically controlled force feedback. To check this, we cleaned the tip by applying a voltage pulse of 5 V when the sample was in contact to the surface. After this we moved to another area and obtained an LC-AFM image shown in Fig. S3c. It can be seen that the current was significantly higher corresponding to an average resistance of 20 kΩ but atomic resolution with trigonal structure still could be observed. At the same time, the locally measured I/V curve (Fig. S3d) changed from a non-linear curve to a linear curve. This indicates that by cleaning the tip we removed the adsorbate layer from the apex of the tip and established a direct contact between the metal atoms and the atoms of the sample surface. Since the tip we used was coated with platinum, which is well known to be an active catalyst, the formation of the adsorbates cannot be avoided even under UHV conditions. On the other hand the existence of an adsorbate layer could also help to stabilize the tip when scanning in contact mode by enlarging the mechanical contact area and thus lower the local pressure (Fig. S3e) as discussed above in detail.

This way, a transition from an indirect contact as in STM to a direct contact between the metallic tip acting as nanoelectrode and the sample can be realized.

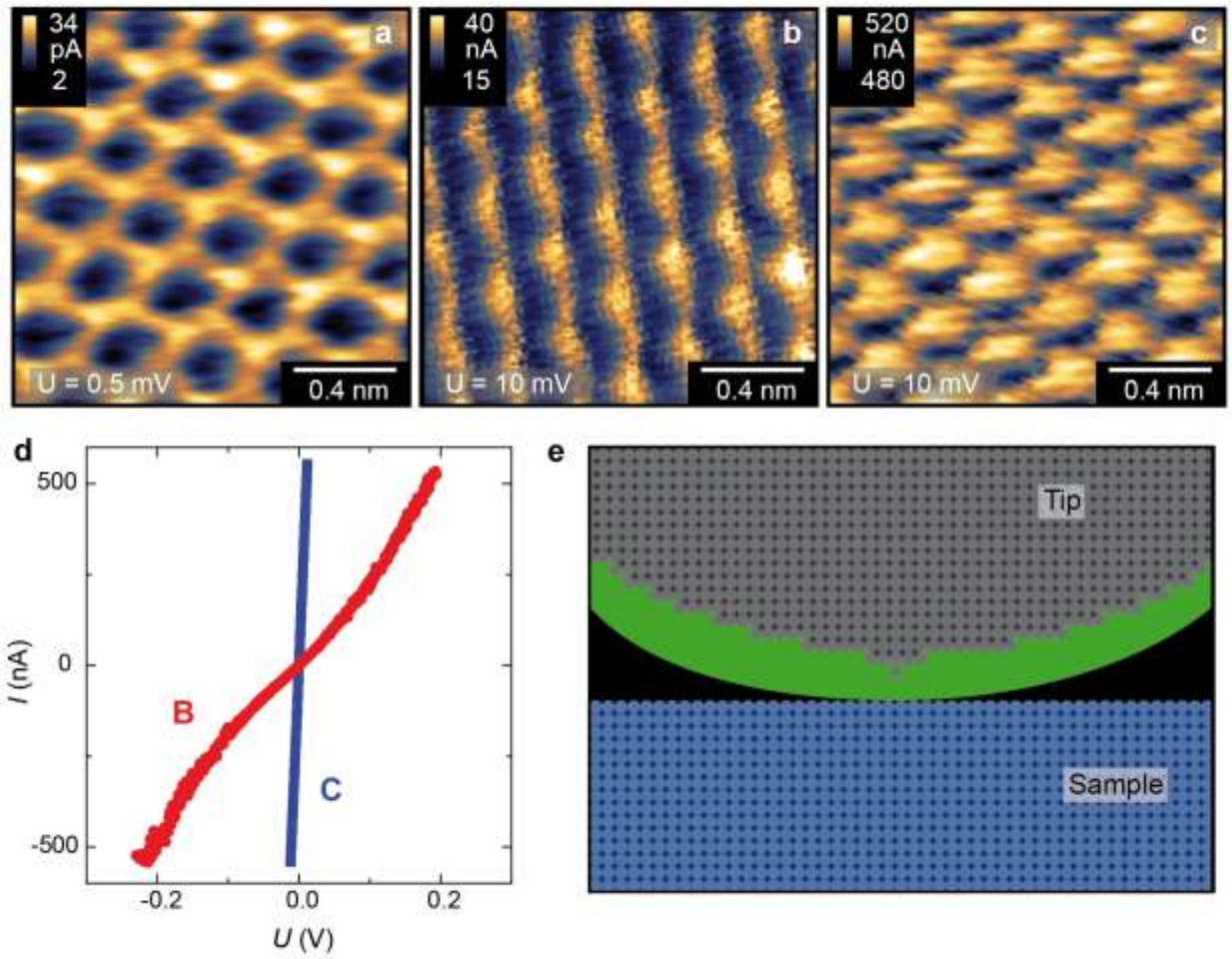

Fig. S3. LC-AFM maps obtained on HOPG using extremely low voltage of 0.5 mV (a) and low voltage (b). Image (c) was obtained using the very same tip as used in image (b) after tip cleaning by a voltage pulse of +5 V. (d) Local I-V curves corresponding to images (b) and (c). (e) Illustration of the contact between tip and sample in case of the presence of an adsorbate layer.

IV. Chemical composition of the surface

The evolution of the chemical composition of the surface during annealing under reducing conditions was analysed by X-ray photoelectron spectroscopy (XPS). The temperature was increased by steps of 100 °C from 500 °C to 900 °C with a dwell time of 1h in UHV before each measurement was started. In Fig. S4, the spectra of the core levels Ti2*p*, O1*s* and C1*s* measured on a TiO_2 (110) surface using excitation by X-rays from an Al Kα source are presented. It can be seen that the TiO_2 spectrum consisted of a single doublet corresponding to the valence state 4+ and did not change significantly within the investigated temperature range. The O1*s* spectrum was simulated by a main peak corresponding to lattice oxygen. Additionally a smaller peak at higher binding energies was present which decreased with reduction temperature and can be attributed to surface adsorbates. In the energy window of the C1*s* line two peaks can be identified which were present only below a reduction temperature of 700 °C. Above this temperature, no carbon signal was measurable indicating that the cleaning of the surface from adsorbates by the thermal annealing was successful. From this measurement we can conclude that the inhomogeneous surface conductivity on the nanoscale as observed by LC-AFM (Fig. 2) is not related to carbon compounds but is a property of the reduced TiO_2 surface itself. Hence we assume that the presence of oxygen vacancies which could form clusters or precursors of linear defects such as Wadsley defects influence the spatial distribution of local surface conductivity strongly.

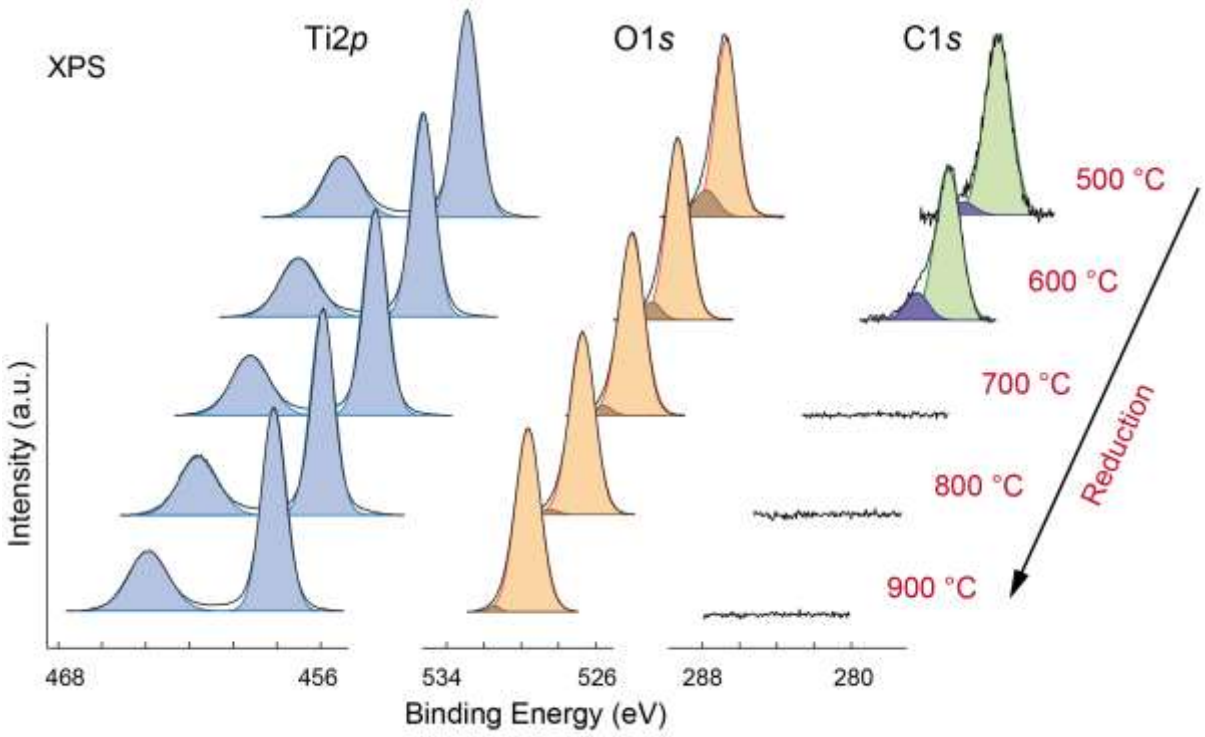

Fig. S4. Spectra of the core levels Ti2*p*, O1*s*, and C1*s* of a TiO_2 (110) single crystal measured by XPS after annealing at different reduction temperatures under UHV conditions.

[1] P. Eyben, W. Vandervorst, D. Alvarez, M. Xu, and M. Fouchier, Springer (2007).
[2] P. De Wolf, J. Snauwaert, T. Clarysse, W. Vandervorst, and L. Hellemans, Appl. Phys. Lett. **66**, 1530 (1995).
[3] R. Holm, Springer (1958).
[4] M. Büttiker, Y. Imry, R. Landauer, and S. Pinhas, Phys. Rev. B **31**, 6207 (1985).
[5] Y. V. Sharvin, J. Exp. Theor. Phys. Lett. **48**, 984 (1965).
[6] A. van der Ziel, Prentice-Hall (1968).
[7] E. H. Rhoderick, Claredon Press (1980).
[8] P. Eyben, S. Denis, T. Clarysse, and W. Vandervorst, Mater. Sci. Eng. B **102**, 132 (2003).
[9] U. Tietze, C. Schenk, and E. Gamm, Springer Berlin Heidelberg (2008).
[10] K. Szot, B. Reichenberg, F. Peter, R. Waser, and S. Tiedke, Springer (2007).
[11] K. Szot, R. Otto, and J. Herion, European Patent, EP 0 789 940 B1 (1999).
[12] J. Pendry, A. Pretre, and B. Krutzen, J. Phys. Condens. Mat. **3**, 4313 (1991).
[13] J. Tersoff and D. R. Hamann, Physical Review B **31**, 805 (1985).
[14] U. Diebold, Appl. Phys. A Mater. Sci. Process. **76**, 681 (2003).
[15] W. Frammelsberger, G. Benstetter, J. Kiely, and R. Stamp, Appl. Surf. Sci. **253**, 3615 (2007).
[16] U. Celano, T. Hantschel, G. Giammaria, R.C. Chintala, T. Conard, H. Bender, and W. Vandervorst, J. Appl. Phys. **117**, 214305 (2015).
[17] J. Perdew and A. Zunger, Phys. Rev. B: Condens. Matter **23**, 5048 (1981).
[18] S. - G. Park, B. Magyari-Koepe, and Y. Nishi, Phys. Rev. B: Condens. Matter **82**, 115109/1 (2010).
[19] B. J. Morgan and G. W. Watson, J. Phys. Chem. C **113**, 7322 (2009).
[20] J. Tersoff and D. R. Hamann, Phys. Rev. Lett. **50**, 1998 (1983).
[21] H. Chen, P. Li, N. Umezawa, H. Abe, J. Ye, K. Shiraishi, A. Ohta, and S. Miyazaki, J. Phys. Chem. C **120**, 5549 (2016).
[22] M. Rogala, G. Bihlmayer, W. Speier, Z. Klusek, C. Rodenbücher, and K. Szot, Adv. Funct. Mater. **25**, 6382 (2015).
[23] H. S. Wong and C. Durkan, Nanotechnology **23**, 185703/1 (2012).
[24] E. Y. Andrei, G. Li, and X. Du, Rep. Prog. Phys. **75**, 56501/1 (2012).
[25] J. Ferrer, A. Martinrodero, and F. Flores, Physical Review B **38**, 10113 (1988).